NANOSIZED MOLECULAR SIEVES

Svetlana MINTOVA

Department of Chemistry, University of Munich (LMU), Butenandtstr. 11 (E), 81377 Munich, Germany; e-mail: svetlana.mintova@cup.uni-muenchen.de

Received June 30, 2003
Accepted July 29, 2003

Nanosized molecular sieves or colloidal zeolites are crystalline porous solids with particle sizes in the range of 10–1000 nm; they are synthesized from colloidal precursor solutions under hydrothermal conditions at temperatures lower than 100 °C. The complex mechanism by which nanosized microporous materials are assembling from framework constituent precursor species under heating is investigated by *in situ* dynamic light scattering, X-ray diffraction using synchrotron radiation, high resolution transmission electron microscopy, and IR/Raman spectroscopies. The development of new crystallization methods that allow the fabrication of zeolites in forms suitable for practical utilization, such as thin films, layers, and monoliths based on the seed method and spin coating approach is discussed. *In situ* X-ray measurements of zeolite crystal growth simultaneously in solutions and films are performed, in which near surface depth-sensitive grazing incidence diffraction is combined with the *in situ* growth of thin zeolite films that is ideally suited to shed light on the unresolved mechanisms of self-organized channel orientation for various zeolite systems. In addition, the nanosized Faujasite (FAU) zeolite was employed as host for the stabilization of guest molecules such as 2-(2′-hydroxyphenyl)benzothiazole (HBT); the trans keto tautomer of HBT inside the FAU zeolite is demonstrated and compared with the cis keto tautomer formed in ethanolic solution.

Keywords: Colloidal zeolites; Molecular sieves; Kinetics; Thin films; Crystal orientation; Crystallization; Dynamic light scattering; X-Ray diffraction; Transmission electron microscopy.

Colloid science plays an important role in numerous industrial technologies and medical applications, such as ceramics, pigments, recording materials, electronics, catalysis, and drug delivery systems. The term “colloids” is used to describe systems that consist of small particles (less than 1 μm); they can be solid or liquid, dense or porous, dispersed or interconnected as supermolecular structures. It is well known that the subdivision of any material into fine particles leads to substantial changes of their properties.

In general, the synthesis of microporous materials is governed by the overall chemical composition of the reactant mixtures and the thermodynamic variables[1]. The zeolite formation process is very sensitive to the ini-

tial reactants, conditions of hydrothermal synthesis and post-synthesis treatments. The synthesis of microporous nanocrystals in the form of stable colloidal suspensions was one of the important events in the zeolite science in the last decade. Although more than 140 types of conventional molecular sieves have been prepared, only several microporous materials, amongst others MFI, MEL, LTA, FAU, LTL, and BEA types have been formed in colloidal suspensions with narrow particle size distribution[2–10]. The synthesis of zeolite crystals with equal particle size requires homogeneous distribution of the viable nuclei in the system. Therefore, the homogeneity of the starting system and simultaneity of the events leading to formation of precursor gel particles and their transformation into crystalline zeolitic material are of primary importance. In order to obtain such homogeneous starting systems, abundant amounts of organic additives and water were employed[8–10]. In addition, the conditions of synthesis required low temperature, below 100 °C, and short crystallization time in order to avoid the Ostwald ripening which leads to formation of big crystallites.

The mechanisms governing the transformation of precursor solutions or gels into zeolitic materials are still a matter of debate and rank among important scientific challenges[11–15]. There is a growing need to understand these mechanisms in order to enhance synthetic control of the design of new zeolite structures, and of the preparation of novel assemblies including films, monoliths, and functional nanostructures. The transformation from amorphous into crystalline microporous nanosized materials have been observed using various techniques such as dynamic light scattering (DLS), nuclear magnetic resonance, small-angle X-ray scattering, and high resolution transmission electron microscopy (HRTEM)[9–25]. However, structure information regarding the initial framework-species assembled from molecular precursors is still very limited.

Besides the fact that the colloidal precursor solutions are very appropriate for *in situ* investigations of the entire process of crystallization, they are also very promising materials for fabrication of different devices. A number of techniques for the fabrication of zeolite-based constructs have been developed, particularly involving the use of nanosized molecular sieves[26–34]. These techniques can be divided into three main groups: (i) direct synthesis of zeolite crystals on a support, (ii) seed method, and (iii) attachment of crystals on functionalized surfaces *via* spin- and dip-coating approaches. However, the film formation process is still not well understood, and it is important to learn how to control this process, in particular the orientation of the zeolite film. The classic method to study bulk structures is X-ray diffraction (XRD). However, standard X-ray diffraction techniques are of lim-

ited value for nanoscale films grown on a substrate. The application of the grazing incidence diffraction (GID) technique permits considerable enhancement of the signal from thin layers relative to the substrate contributions. The orientation of the crystals along the film thickness can be detected *via* changing the incident and exit angles of the X-ray beam and collecting the Bragg reflections at different penetration depths[35].

In addition, novel nanostructured functional materials can be constructed *via* encapsulation of optically active guests in microporous hosts. Incorporation of organic molecules inside the cages of zeolites will permit the control of both their molecular and optical properties. Moreover, colloidal molecular sieves with particle sizes in the nanometer range can have high colloidal stability in different solvents with respect to further agglomeration and sedimentation. These features also make the encapsulation of functional optical molecules in nanoscale zeolite suspensions an attractive synthetic target[36–38].

The present paper covers the synthesis and characterization of stable colloidal suspensions of discrete zeolites, with emphasis on the complex mechanism by which they assemble from framework constituent precursor species under hydrothermal synthesis conditions. Different methods for fabrication of thin zeolite films based on nanosized crystals including seed approach and spin coating will be discussed. In addition, the structure evolution of nanoscale zeolites simultaneously in solutions and films was studied by grazing incidence diffraction using synchrotron X-ray radiation. A possibility to incorporate organic dyes in nanoporous host is demonstrated.

RESULTS AND DISCUSSION

Synthesis of Nanosized Molecular Sieves from Colloidal Precursor Solutions

Study of the entire process of nucleation and crystal growth is carried out in precursor solutions resulting in crystallization of a large-pore molecular sieve (Beta) with BEA type structure[39] (Table I). This material is a promising catalyst for many reactions because it can be prepared with various Si/Al ratios and different particle sizes. Nanosized Beta crystals were synthesized from two colloidal precursor solutions having the following chemical composition:

Solution B1: 0.25 Al_2O_3:1.0 SiO_2:0.2 $(TEA)_2O$:11.8 H_2O
Solution B2: 1.0 SiO_2:0.2 $(TEA)_2O$:11.8 H_2O.

The silica source for the preparation of the initial precursors was freshly freeze-dried colloidal silica Ludox SM 30 (30 wt.%), aluminium isopropoxide, and the alkali source was tetraethylammonium hydroxide (TEAOH; 20 wt.% in water). These components were mixed under vigorous stirring and aged on an orbital shaker at ambient temperature for 24 h prior to the further hydrothermal (HT) treatment at 100 °C. The nanosized crystals resulting from the HT treatment of colloidal solutions were purified by separation from the mother liquor by three-fold of centrifugation (20 000 rpm, 60 min). After each step the nanoparticles were redispersed in doubly distilled water using an ultrasonic bath for 2 h.

The crystallization process of zeolite Beta was followed by *in situ* dynamic light scattering with an ALV-NIBS/HPPS instrument. The back scattering geometry of the DLS (scattering angle 173°, HeNe laser with 3 mW output power at 632.8 nm wavelength) allows measurements at high sample concentrations, therefore all analyses were performed on samples having the original concentration without any pretreatment of the colloidal mixtures. The back scattering of light produced from these X-ray amorphous samples was strong enough to be monitored as a function of the particle numbers and particle mass. The mean particle radius (r) is calculated according to the equation: $r = k_B T/6\pi\eta D$, where k_B is the Boltzmann constant, T is the actual temperature of the dispersion, η is the solvent viscosity, and D is the diffusion coefficient. The radius calculated from this relation is known as hydrodynamic radius since it relies on the Stokes coefficient, $6\pi\eta r$, a result from fluid or hydrodynamics[40]. The cumulant analysis gives an average particle radius, which is located between the minimum and maximum particle sizes present in the sample. For the precursor colloidal solutions B1 and B2

TABLE I
Structural characteristics of zeolites[39]

Zeolite	Framework type code	Channel dimensions[a]
Zeolite A	LTA	<100> **8** 4.1 × 4.1 Å ***
Zeolite Y	FAU	<111> **12** 7.4 × 7.4 Å ***
Silicalite-1	MFI	{[100] **10** 5.1 × Å ↔[010] **10** 5.3 × 5.6 Å}***
Beta	BEA	<100> **12** 6.6 × 6.7 Å** ↔[001] **12** 5.6 × 6.7 Å*

[a] Number of **T**-atoms (in bold type) forming the rings (channels); the channel direction (relative to the axes of the type material structure); free diameter of the channels in Å; number of asterisks indicates whether the channel system is one-, two- or three-dimensional; interconnected channel systems are separated by a double arrow (↔).

it is found that the mean radius increases from 6 to 60 nm with increasing aging and heating times (Fig. 1). The value of the polydispersity index also increases in the same direction, suggesting a multimodal particle size distribution in these samples with time. As the value of the polydispersity index is significantly larger than 0.2 and the calculated hydrodynamic radius is no longer reliable, independent distribution function analyses are required for these samples. Figure 1 shows the particle size distribution data of samples B1 and B2 heated for 80 and 400 h, respectively. The presence of subcolloidal particles with size in the range *ca* 2–8 nm is measured in both samples during the first several hours of heating. After 40 and 20 h for solutions B1 and B2, respectively, an increase in the scattering intensity due to the presence of second-generation particles with radius of *ca* 60 nm is observed (Fig. 1). A similar trend can be extracted from the distribution func-

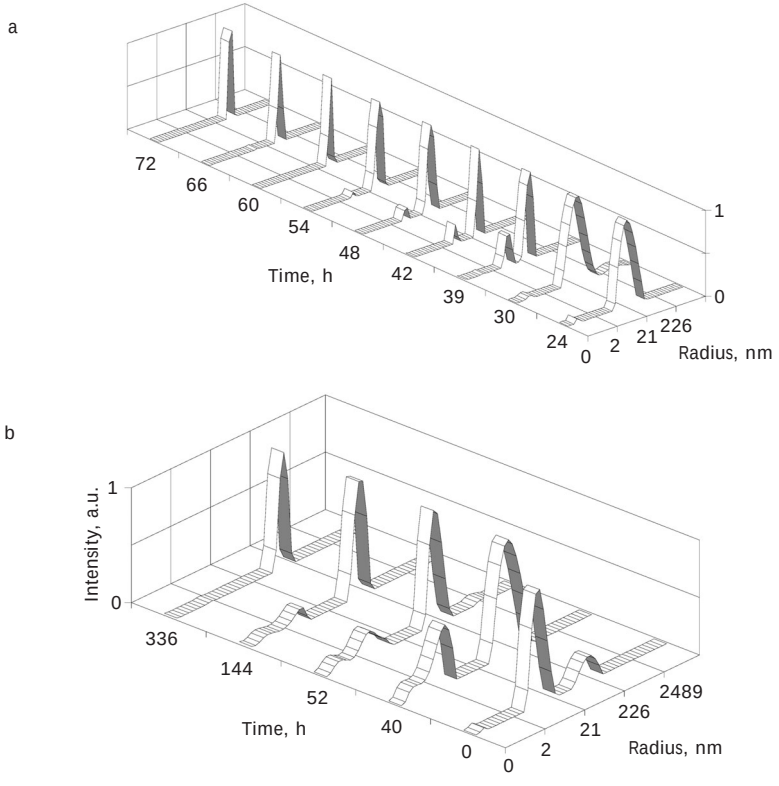

FIG. 1

DLS data of B1 (a) and B2 (b) precursor solutions heated at 100 °C for 80 and 400 h, respectively. The DFA is displayed as scattering intensity per unweighted particle size classes

tion analysis (DFA) data plotted as a function of the mass distribution. Further evolution of the two mixtures depends on the temperature treatment. A milky suspension is obtained after hydrothermal treatment of the B1 and B2 solutions for 60 and 330 h, respectively, but no sedimentation of the crystalline product is visible after prolonged hydrothermal treatment. The final samples contain particles with unimodal size distribution; a mean hydrodynamic radius of 60 nm is measured in both solutions (Fig. 1a and 1b). The XRD analysis of the purified and freeze-dried samples synthesized from solution B1 is presented in Fig. 2. The results confirmed that the Beta-type molecular sieve was completely crystalline after 72 h of hydrothermal treatment of the precursor solution, while the sample heated only for 27 h shows no crystalline reflections. Comparing the results obtained by DLS and XRD, one could conclude that with decreasing fraction of subcolloidal particles, the crystallinity of the sample increases; the amorphous phase is a function of the amount of 6-nm subcolloidal particles. The corresponding light scattering data suggest that the zeolite phase is represented by the particles with a radius of 60 nm, while the smaller fractions (≈6 nm) are still amorphous.

Further supporting evidence related to the structure of the nanosized particles in the precursor solutions is obtained from IR spectroscopy. Freeze-dried samples were prepared from the B1 synthesis solution, which still appeared clear after 27 and 36 h, and from the milky suspension after 72 h of hydrothermal treatment. Three vibrational bands in the region of 400–700 cm^{-1} characterize the IR spectrum of pentasil-type molecular sieves. The

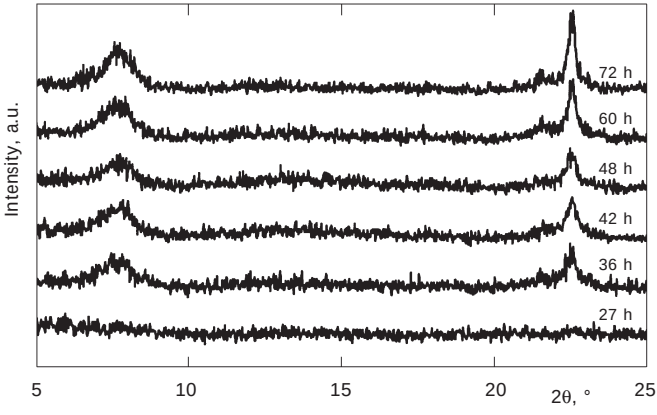

FIG. 2
XRD patterns of Beta nanocrystals synthesized from solution B1 under HT treatment at 100 °C

first band at 440–470 cm^{-1} is a Si–O bending mode observed in amorphous SiO_2 materials, and the other in the region of 520–580 cm^{-1} indicate the double five-membered rings existing in the pentasil zeolite structure[41]. Distinct absorptions appear at 457 and 576 cm^{-1} in the spectrum of the X-ray amorphous sample heated only for 27 h (Fig. 3a). The second band is very broad; with increasing crystallization time up to 36 h, the sample contains two well-resolved and sharp bands at 522 and 574 cm^{-1}, which are usually observed in a very crystalline silicate sample (Fig. 3b). These data confirm that already at a very early stage of the synthesis, the architecture of Beta is possibly formed even after 27 h. Although this sample is X-ray amorphous, the IR spectroscopic data suggest that the crystals already nucleate and grow into the colloidal particle detected by DLS (see Fig. 1). The intensity and positions of the two bands at 522 and 574 cm^{-1} are similar for both samples heated for 36 and 72 h, which demonstrates a high degree of crystalline order.

The TEM images reveal the presence of solid objects with a mean diameter of *ca* 50 nm and with a typical amorphous appearance, after mixing of all compounds and aging for 24 h (Fig. 4a). The appearance of the first crystalline fringes confirmed the formation of the Beta crystalline structure in the precursor solution after 36 h of hydrothermal treatment (Fig. 4b). The particles are very stable during the purification of the samples including one-step centrifugation and ultrasonic re-dispersion in doubly distilled water. With further increasing the heating time up to 72 h, no big difference in

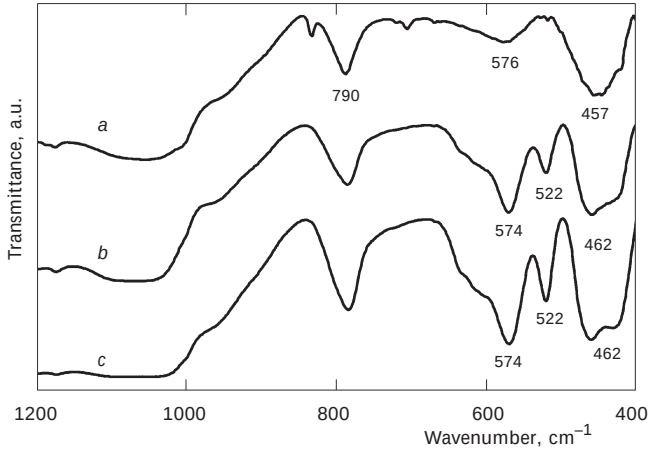

FIG. 3
IR spectra of samples synthesized from solution B1 at 100 °C after 27 h (*a*), 36 h (*b*), and 72 h (*c*)

the final particle size of the polycrystalline zeolite Beta is observed. The crystalline fringes were visible in all grains and no amorphous particles were observed (Fig. 4c). The crystallization behavior of zeolite Beta from pure siliceous and aluminosilicate solutions is similar, only a difference in the kinetics is observed. The crystallization process takes a longer time for pure silica zeolite Beta (about 400 h) compared with the aluminosilicate Beta sample (72 h).

In conclusion, nanosized Beta zeolite is synthesized from pure siliceous and aluminosilicate colloidal precursor solutions under hydrothermal conditions. A DLS study reveals that in the precursor solutions two main particle size classes with hydrodynamic radii of *ca* 6 and 60 nm are formed during heating. The small subcolloidal particles are consumed during the first several hours of heating and transformed into crystalline Beta particles after 60 and 400 h for the solutions B1 and B2, respectively. The IR spectra reveal the presence of small silicate units containing possibly double five-membered rings corresponding to the secondary building units in this zeolite even in the X-ray amorphous sample and well resolved and sharp bands in the fully crystalline colloidal Beta sample. The mean radius of the final Beta crystals is *ca* 60 nm for both the pure silica and aluminosilicate samples. Probably the size and the unimodal particle size distribution in these samples are dependent on the degree of supersaturation, which is determined from the amount of the organic additive (TEAOH) and water content. In both systems the amounts of water and organic additive are kept constant and the used silica source is freshly dried colloidal silica.

A combination of IR spectroscopy and HRTEM with the DLS technique provides details about the early stages of amorphous particles formation and entire zeolite crystallization.

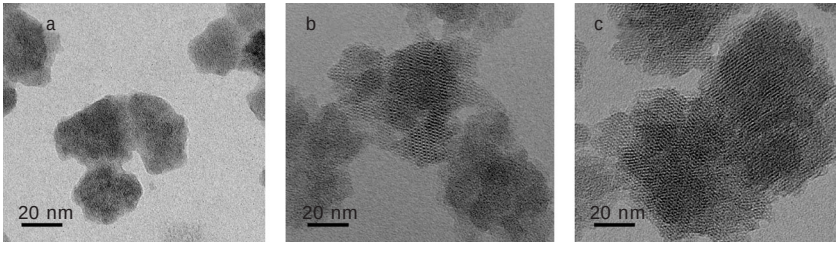

FIG. 4
TEM micrographs of nanocrystals obtained from solution B1 after aging at room temperature for 24 h (a), and hydrothermal treatment at 100 °C for 36 h (b) and 72 h (c)

Preparation of Thin Films Based on Nanosized Molecular Sieves

Nanosized molecular sieves can be used as building blocks for the preparation of thin microporous films, monoliths and two- and three-dimensional constructs[27–31]. The preparation of thin films based on pure silica MFI-type molecular sieve on silicon wafers *via* two approaches, *i.e.*, spin-coating and seed methods, is demonstrated.

Zeolite seeds having MFI-type structure with an average size of 30 and 60 nm were synthesized from pre-hydrolyzed synthesis solutions with the following chemical compositions:

Solution S1: 9 TPAOH:25 SiO_2:408 H_2O:100 EtOH
Solution S2: 5 TPAOH:25 SiO_2:408 H_2O:100 EtOH.

The silica source used for preparation of the above solutions was tetraethoxysilane (TEOS; 98%) and the organic template was tetrapropylammonium hydroxide (TPAOH; 1 M aqueous solution). After hydrothermal treatment of the precursor solutions at 90 °C for 15 h, the seed crystals were purified in three-fold of high-speed centrifugation with a Sorvall T21 (20 000 rpm for 1 h) and redispersed in distilled water under ultrasonication (2 h). The seed-sols containing MFI crystals with the dry matter content 3 wt.% and pH 10 were prepared and further used for the formation of adsorbed MFI monolayers.

The first approach used for preparation of MFI films on silicon wafer is called the seed method (Fig. 5). This method involves three main steps: (i) a deposition of cationic polymer (Redifloc 4150, Akzo Nobel), (ii) adsorption of crystal seeds on the positively charged silicon surface, and (iii) additional crystal growth of the seeded layer under hydrothermal conditions. The additional hydrothermal treatment was carried out at 90 °C for 6–30 h in order to induce further growth of the seeded crystals into dense and thick films. Both the adsorbed and the grown zeolite films were calcined at 450 °C for 3 h in air to remove the organic template prior to further measurements.

In addition to the seed method, a spin-coating approach was used for preparation of MFI-type films on one-side polished silicon wafers. A typical spin coating procedure is shown in Fig. 6; the resulting films were prepared from the two coating mixtures S1 and S2. In order to prepare stable coating mixtures for deposition of films *via* spin coater after the third purification step, the zeolite particles were redispersed in ethanol ensuring a concentration of the solid nanocrystals in the final suspensions of *ca* 3 wt.%. The size of the substrates was varied from 10 to 150 mm, and plates were mostly

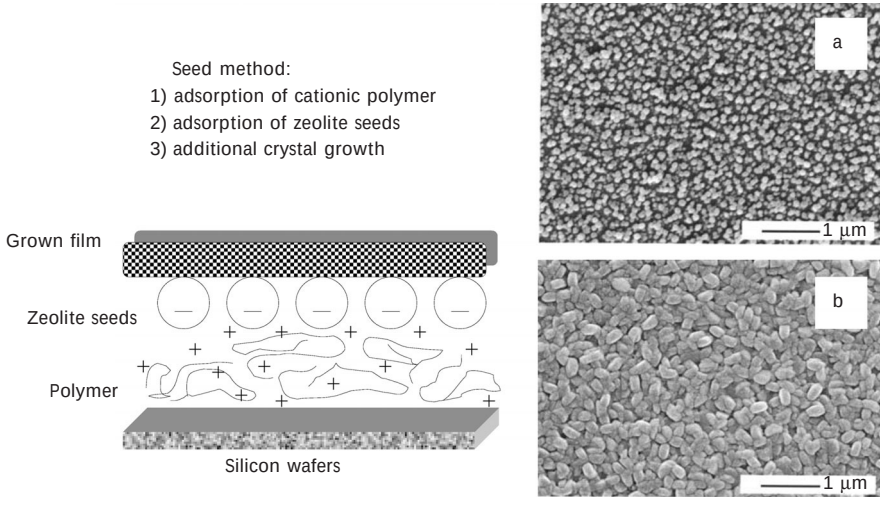

FIG. 5
Schematic representation of the seed approach used for preparation of MFI films on silicon wafers; MFI films after adsorption of nanosized seeds (a) and additional crystal growth (b)

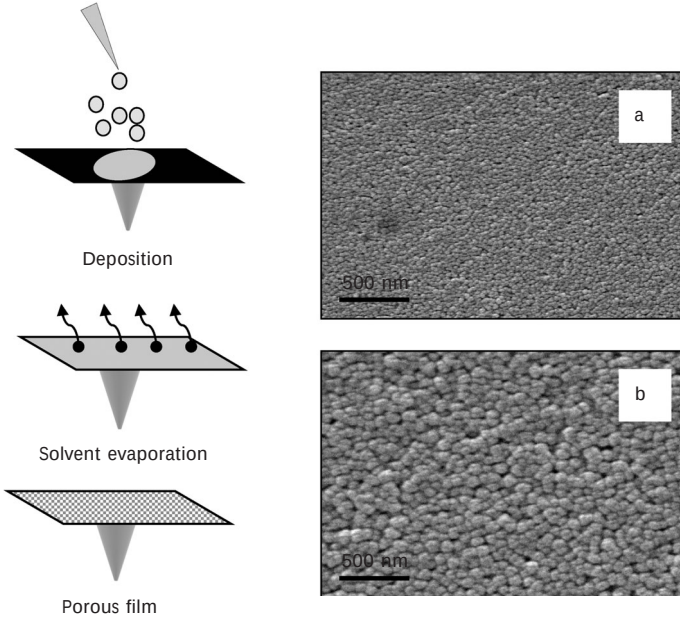

FIG. 6
Schematic representation of the spin coating approach used for preparation of MFI films on silicon wafers; MFI films prepared from solutions S1 (a) and S2 (b)

round, but also non-regular like square and rectangular shapes were covered with nanosized molecular sieve layers. The substrates were vacuum-locked during the spin-coating process. A chemical substrate cleaning procedure was applied for 10 s with two different solvents – ethanol and acetone. Uniform coatings with the thickness in the range 150–500 nm were prepared at an acceleration rate of 1000 rpm s^{-1} and the spinning rate in the range 1000–3000 rpm for 35 s. An additional spin-coating step with the solution S1 or S2 formed the multilayered zeolite films.

The structural properties of MFI films, *i.e.* the orientation of the crystallites, were investigated by measuring Bragg reflections with the reciprocal lattice vector parallel to the samples surface. The scattering geometry for grazing incidence diffraction is shown in Fig. 7. The depth sensitivity in the growth direction is obtained by changing the incident (α_i) and/or exit (α_f) angles, which are of the order of the critical angle (α_c) for total external reflection, typically some tenths of degree. The incident angle was varied in order to change the scattering or "information" depth (L) from *ca* 7 to 500 nm. The penetration depth for $\alpha_i < \alpha_c$ is determined by refraction effects, while for $\alpha_i > \alpha_c$, L is controlled by photoabsorption. The Bragg intensity as a function of the exit angle α_f is collected by a position-sensitive detector (PSD) placed perpendicular to the samples surface[44] as well as with CCD. The wavelength used was selected by a double crystal monochromator from the undulator spectrum of beamline ID 10b at the ESRF, in Grenoble. The footprint on the samples surface is about 0.5 × 0.5 mm^2 given by the cross-section of the parallel incident beam and the collimated beam behind the sample.

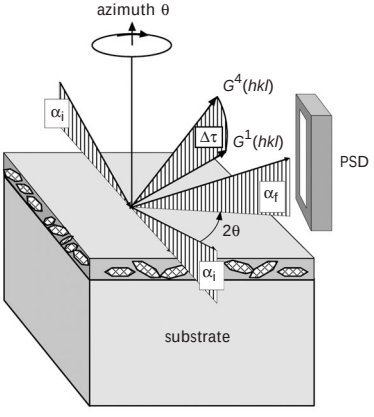

FIG. 7
Scattering geometry of grazing incidence diffraction in real space

In our experiments, the key features of the structure of the MFI layers on the silicon substrate are obtained from the specific direction measured in reciprocal space. The radial direction Q_{radial} scanned by varying the scattering angle 2θ, and yields the Bragg angles of all structurally allowed G_{hkl}. Most important for the texture determination of the MFI crystallites is the intensity ratio of (101) and (011), (200) and (020), (501) and (051), and (033) and (303) reflections[45]. In the pore system of the MFI-type structure, the straight channels are parallel to the *b*-axis whereas sinusoidal channels extend along the *a*-axis (Fig. 8). The dimensions of the straight and sinusoi-

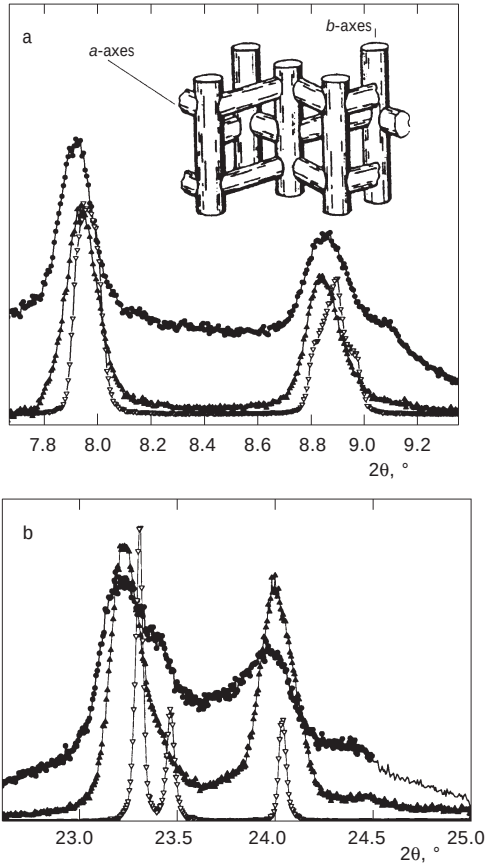

FIG. 8

Radial 2θ-scans of a spin-coated film from solution S1 (●), solution S2 (▲) and grown film prepared by seed method (▽): in the 2θ range 7–10° (a) and 22–25° (b). The angle of incidence is kept constant at α_i = 0.1°. Inset: the topology of the channel system of MFI-type molecular structure

dal channels are 0.53 × 0.56 and 0.51 × 0.55 nm, respectively (Table I). The orientational distribution of the corresponding channels is most directly imaged in the α_f-spectra at these specific Bragg reflections as explained above. The incident angle was kept constant to 0.1° and the scattered intensity was integrated over all channels of the PSD, thus covering an angular range in α_f of about 2°. The Bragg peaks recorded from the spin-coated films (solutions S1 and S2) and from the grown film are shown in Fig. 8. The peaks are intensive and shifted from (101) to (011) and from (200) to (020) in the low-angle region from spin-coated to grown films (Fig. 8a). In the angular range, 2θ = 22–25°, we find the pronounced peaks, which for grown films are indexed by (051/–501) and (033/–303), while for spin-coated films the (*hkl*) values are (501) and (303). The crystals in the grown films are oriented predominantly with *a*-axis perpendicular to the substrate because all the detected Bragg reflections have (*hkl*) values with *h* = 0. After correcting the half-width of the peaks for the instrumental resolution, and attributing the remaining width to size broadening only, we determined the diameter (*d*) of the crystallites, using the Sherrer relation $d = \lambda/\cos\theta\,\Delta 2\theta$, and these results are consistent with the SEM results. According to the calculated data, the spin-coated crystals have sizes about 60 nm (Fig. 6), while in the grown films larger, intergrown crystals and aggregates in the range 300–400 nm were formed (see also Fig. 5b). It is also clear that a large fraction of the crystals in the grown films are oriented with their *a*-axes directed perpendicular to the substrate surface, since the (0*kl*) peaks are the most intensive ones but also some peaks with (*h*0*l*) values are present (see Fig. 8). More randomly oriented crystals are deposited in the multi-layered film obtained after two-step spin coating of the S1 and S2 suspensions since the main Bragg peaks with (*hkl*) values equal to (200), (020), (501), (051), (133), and (104) are observed (figure is not shown). From the above results it could be concluded that the orientation of the crystals in the microporous films depends mainly on the morphology of the nanosized crystals and it is responsible for the different crystal orientations. The preferred orientation of the crystals could be also controlled by using different methods of film deposition and by changing the conditions for preparation, *i.e.*, spin rate, crystallization time, coating sol concentration, *etc.*

In our experiments, the key features of the MFI films were also obtained from GID measurements recorded with CCD for the grown film at two different incident angles of the X-ray beam (Fig. 9). Debye–Scherrer rings without any maximum along the ring are typical of powder-like samples, while pronounced maxima on the rings indicate a preferential orientation of the crystals in the film. An intensive maximum located on the Debye–Scherrer

rings in Fig. 9a indicates that most of the crystals in the layer at penetration depth of *ca* 270 nm (α_i = 0.3) are oriented with the *b*-face perpendicular to the substrate. Similar measurements were carried out at incident angles of 0.05, which corresponds to penetration depths of *ca* 8 nm (see Fig. 9b). It is apparent that the growing crystals follow the orientation of the seeds during the HT treatment. A lower order of the nanocrystals at the surface of the film is observed. Obviously the seeds have a strong effect on the film orientation at first stages of film growth. With increasing film thickness, this effect becomes less pronounced and the MFI crystals in the top layer are randomly oriented.

In conclusion, the preparation of MFI-type films by one single or multiple spin-coating processing steps and seed approach on silicon wafers is demonstrated. The spin-coating process can be performed one or several times in order to increase the thickness and possibly the packing density of

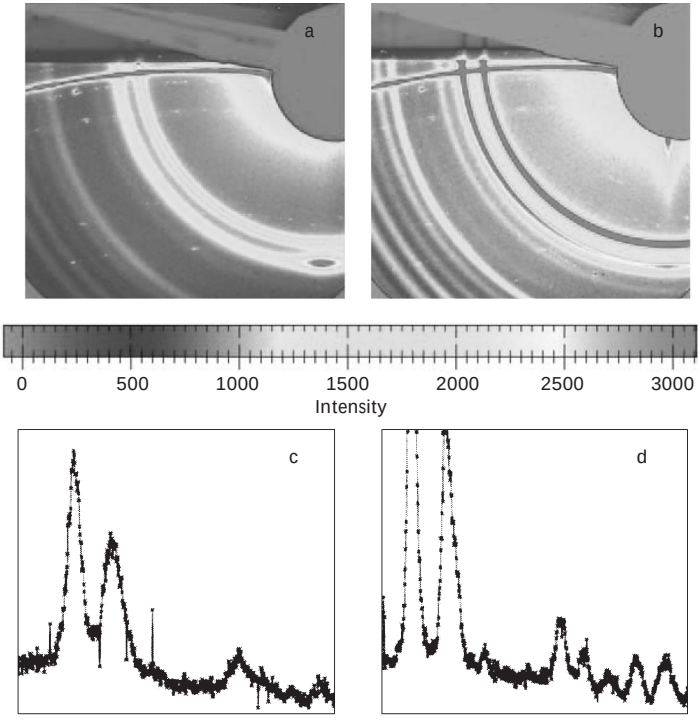

FIG. 9

CCD images of the MFI nanocrystals in grown film at incident angle α_i = 0.3° (a) and α_i = 0.05° (b), and the XRD profiles extracted from these images at α_i = 0.3° (c) and α_i = 0.05° (d). X-Ray energy 15 keV, wavelength 0.0827 nm

the film. The fact that pre-synthesized porous nanoparticles can be used for the preparation of the films implies that almost any substrate can be covered with MFI-type zeolite and other porous materials (some of which might not be accessible under direct growth conditions). Preferred orientation of porous materials in the spin-coated films can be obtained by applying non-spherical MFI-type particles and one or several deposition steps. The present method is particularly suitable for applications requiring rapid deposition of porous thin films under gentle processing conditions, including sensor devices, optical coatings, catalysts, and low-*k* dielectric layers.

In Situ Study of Crystal Growth of Nanosized Zeolites Simultaneously in Solutions and on Substrates

Structural control on the nanometer scale is one of the most fascinating and important goals of modern solid-state and materials chemistry. The experimental methods used to investigate the underlying kinetics of zeolite crystal growth include *ex situ* techniques such as X-ray diffraction, SEM, IR spectroscopy, and HRTEM of solids withdrawn during the synthesis, and the *in situ* examination of the synthesis solution by DLS and various spectroscopic techniques. However, the process of zeolite crystal growth in solutions and film formation is still not well understood.

A new strategy for *in situ* GID measurements of the crystal growth of nanosized zeolite in films and simultaneously in solution is developed. This approach allows for the investigation of thin zeolite films with different thicknesses on any kind of planar substrates placed in the precursor solution from which the films grow.

The *in situ* investigation of crystal growth of LTA-type zeolites (Table I) is performed and shown here. The synthesis mixtures used for the preparation of stable colloidal suspension of LTA nanocrystalline seeds had the following chemical composition:

Solution A: 0.35 Na_2O:11 SiO_2:1.7 Al_2O_3:13 $(TMA)_2O$:500 H_2O.

The LTA seed films were prepared *via* spin coating approach on glass plates; a uniform seed layer from zeolite nanocrystals with a thickness of *ca* 50 nm was formed at an acceleration rate of 1000 rpm s^{-1} and a spinning rate of 2500 rpm for 35 s with the coating suspension. Additional growth of the LTA-seeded crystals in films and in solution was carried out in a specially designed container (Fig. 10Aa) at 60 °C for 14 h. The reactor shown in Fig. 10Aa absorbs only 30% of the intensity transmitted along the 10 mm path

through the suspension at X-ray energy of 15 keV. In order to place the incoming X-ray beam either on the film or in the surrounding solution, the sample container was moved from position 1 to 2. The scattered intensity is collected at small α_f by a position-sensitive detector as a function of the scattering angle 2θ (Fig. 10Ab). A well-collimated X-ray beam strikes the sample surface under a small incident angle of the order of the critical angle for total external reflection. Experimental results for nanocrystals growing in solutions and on the seeded glass plate are shown in Fig. 10B. In the case of the LTA suspension containing small randomly distributed crystallites, a diffractogram similar to a powder pattern is expected and observed as shown in Fig 10B, curve *1*. For the same scan, repeated with the film in

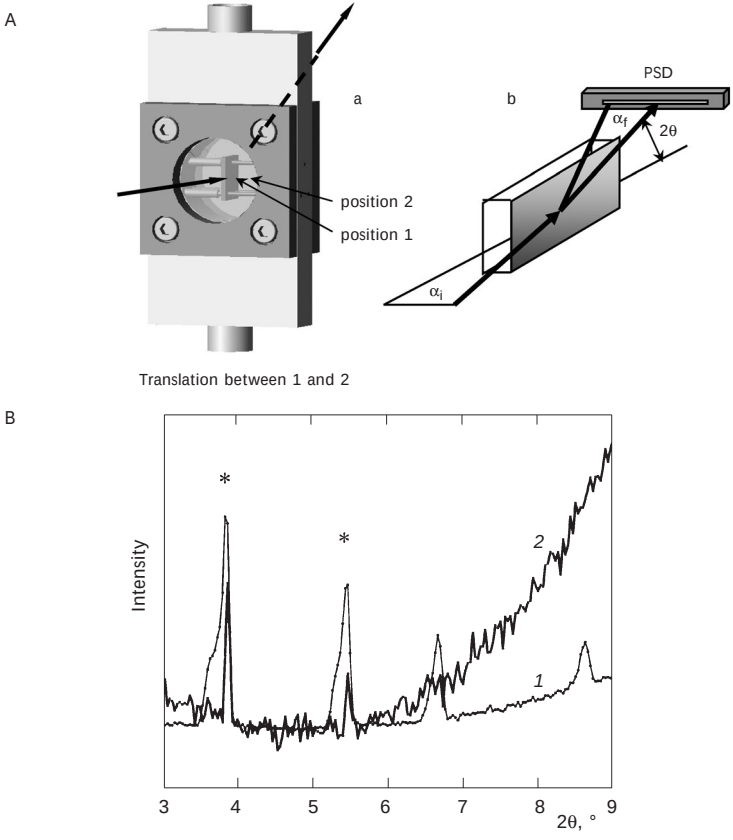

FIG. 10

A – Sample container for: a *in situ* X-ray measurements of zeolite crystal growth on film (position 1) and in solution (position 2), b the scattering geometry in GID. B – Radial 2θ-scans of the LTA crystals in suspension (*1*) and in the zeolite film (*2*) in GID geometry in the 2θ range 3–9°

the beam (position 1, Fig. 10Aa), two Bragg reflections with a symmetric peak shape and weaker intensities are found with (*hk*0) values of (200) and (220) (see Fig. 10B, curve *2*). Both observations confirm that the LTA nanosized particles are oriented with the *c*-axis perpendicular to the sample surface. Additional depth sensitivity is achieved when the intensity distribution along the α_f is investigated. For different α_i, the "α_f spectra" reflect the distribution of the crystal orientation as a function of depth. In the case of the zeolite suspension, a uniform intensity is found because the position-sensitive detector records a section of the Debye–Scherrer ring corresponding to the powder-like nature of the crystallites in the suspension. The "α_f spectrum" recorded from the film looks completely different; a sharp pronounced maximum is found, sitting on an otherwise constant background resulting from the remaining scattering of the zeolite suspension (not shown). The peak has a maximum at the critical angle of 0.02 and decays quickly for larger α_f values. Both features described above are characteristic of single crystals or highly oriented crystallites with the reciprocal lattice vector being parallel to the sample surface.

In situ X-ray measurements of zeolite crystal growth in solutions and films based on depth-sensitive grazing incidence diffraction study are ideally suited to shed light on the unresolved mechanisms of self-organized channel orientation for various zeolite systems. The change of zeolite crystal orientation within the film structure could be followed with the high depth-sensitivity of the GID technique, and it is possible to examine the crystal growth of nanozeolites in precursor colloidal suspensions during the first several hours of hydrothermal treatment.

Zeolite Nanocrystals as Hosts for Incorporation of Dyes

Novel nanostructured functional materials can be constructed *via* encapsulation of optically active guests in microporous nanosized hosts. Incorporation of organic molecules inside the cages of zeolites would permit the control of both their molecular and optical properties. These features make the encapsulation of functional optical molecules in nanoscale zeolite suspensions an attractive synthetic target. Such suspensions are (i) promising systems for optical investigations of host-guest interactions and (ii) interesting precursors for the construction of nanostructured assemblies such as optical coatings and selective chemical sensors.

In situ incorporation of hydroxybenzothiazole (HBT) inside the supercages of nanosized large-pore FAU zeolite as a co-template from a precursor colloidal solution is demonstrated.

Nanosized HBT-FAU and pure FAU crystals (Table I) were prepared from clear precursor solutions with the following molar compositions:

FAU sample: 5.5 $(TMA)_2O$:2.3 Al_2O_3:10 SiO_2:570 H_2O
HBT-FAU sample: 0.05 HBT:2.7 $(TMA)_2$:2.3 Al_2O_3:10 SiO_2:100 H_2O:400 EtOH.

Starting mixtures are prepared from tetramethylammonium hydroxide pentahydrate ($TMAOH \cdot 5H_2O$), aluminium isopropoxide and colloidal silica (SiO_2, 30 wt.%). The final precursor solutions were aged on an orbital shaker (180 rpm) at room temperature for 24 h prior to further crystallization at 90 °C. The crystalline structures were determined by XRD, while the degree of loading was confirmed with thermogravimetric measurements. *In situ* dynamic light scattering was used to investigate the particle size distributions at room temperature and upon HT treatment in both systems resulting in the formation of FAU and HBT-FAU samples. Raman spectra for purified and freeze-dried samples, and time-resolved absorption and emission spectra of the samples stabilized in ethanolic solution were collected.

According to X-ray powder diffraction analysis, both samples correspond to the FAU zeolite-type structure (Fig. 11)[45]. The TEM image of pure FAU sample shows well-defined octahedral crystals with size of about 60 nm and crystalline fringes corresponding to the FAU structure. DLS data reveal that the FAU and HBT-FAU zeolite suspensions contain only monodisperse par-

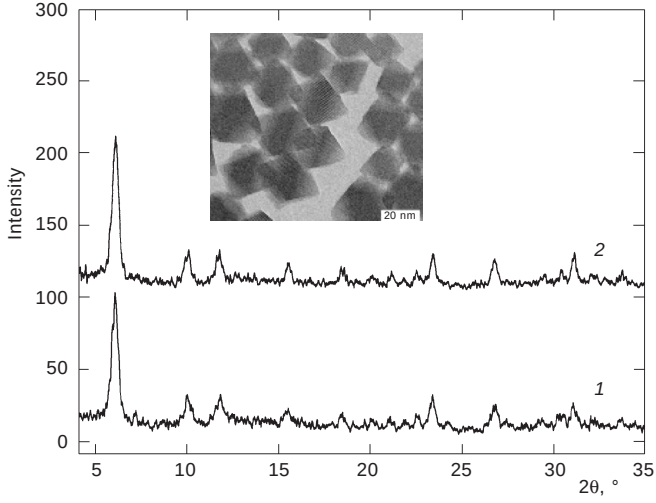

FIG. 11
X-Ray patterns of pure FAU (*1*) and HBT-FAU (*2*) nanocrystals. Inset: TEM image of pure FAU nanocrystals

ticles with a mean hydrodynamic radius of 60 and 70 nm, respectively. The crystallization behavior of FAU crystals is the same in both solutions with and without of HBT. The presence of only colloidal particles with a mean radius of about 8 nm and broad particle size distribution were found in the HBT-FAU sample after 40 min aging at room temperature (Fig. 12). After HT treatment for 45 h, an increase in the scattered intensity due to the presence of a second generation of particles with radius of about 70 nm is observed. When increasing the HT treatment to 70 h, the small fraction (≈8 nm) is consumed and transformed completely into 70 nm particles (Fig. 12). A similar trend can be extracted from the DFA data plotted for pure FAU sample (data are not shown).

In order to characterize the environment of HBT and to provide experimental evidence for the incorporation of HBT within the FAU nanosized crystals, Raman spectra of pure FAU and HBT-FAU samples were recorded (figure is not shown). Both spectra are dominated by the Raman lines assigned to the presence of TMA^+ cations[46]. Moreover, in the spectrum of the HBT-FAU sample, numerous new lines due to the presence of HBT in the zeolite are observed. For example, three Raman lines of HBT incorporated within the FAU nanocrystals at 1343, 1433 and 1478 cm^{-1} are associated with the enol-HBT lines in ethanol solution at 1320, 1440 and 1464 cm^{-1}, respectively[47]. The Raman data confirm the presence of HBT in the HBT-FAU sample and also reveal a modification of the TMA^+ environment when the faujasite is synthesized in the presence of HBT. The presence of double lines around 750 and 950 cm^{-1} reflects the existence of two different conformations of TMA^+ in the FAU structure, while only two single lines at

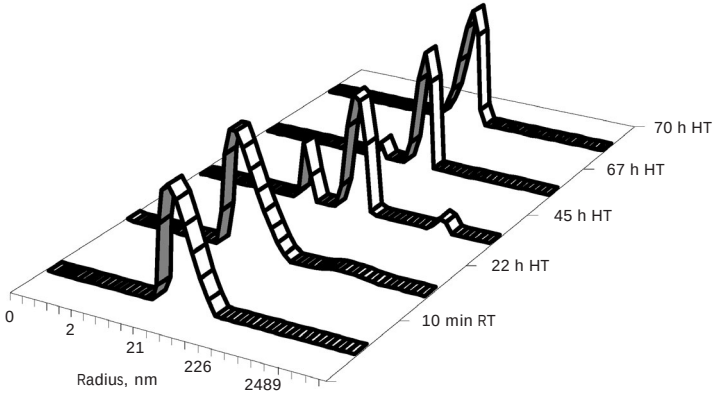

FIG. 12
DLS data of precursor solution HBT-FAU heated at 90 °C for 70 h. The DFA is displayed as scattering intensity per unweighted particle size classes

755 and 955 cm^{-1} are observed in the Raman pattern of HBT-FAU. This observation suggests that only one conformation or local environment of TMA^+ is present in HBT-FAU. In order to probe the association of HBT and TMA molecules with the pure FAU and HBT-FAU samples, thermogravimetric analysis of washed and freeze dried samples was performed (Fig. 13). The weight loss of the FAU sample in the temperature range 200–600 °C is 6 wt.%, due to combustion of TMA (weight loss below 200 °C is attributed to the removal of zeolite-type water). The TMA template in pure FAU decomposes in at least two steps, at 420 and 510 °C, which may suggest different local environments of the TMA template in the FAU structure. In contrast to the pure FAU sample, the thermal degradation of TMA and HBT occurs predominantly at 450 °C (9 wt.%). These results point to the different local environments of the organic molecules in the two samples, which is consistent with the Raman data.

In conclusion, the dye 2-(2′-hydroxyphenyl)benzothiazole was successfully incorporated into the voids of nanoscale FAU zeolites. The mechanism of inclusion appears to involve a complex interaction between TMA^+ and HBT occurring during the templating phase of the synthesis. In addition, the UV-VIS spectroscopic data reveal the stabilization of the trans keto tautomer of HBT inside this large-pore molecular sieve. The trans keto tautomer exhibits highly intensive fluorescence in the zeolite, as compared with the cis keto tautomer formed in the ethanol solution. The time-resolved measurements reveal an increase of the fluorescence around 470 nm within

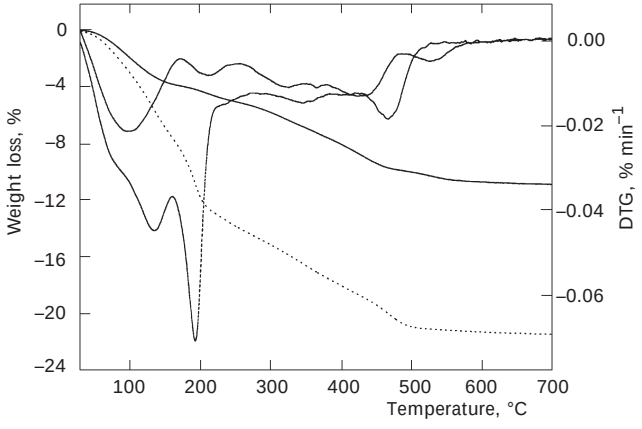

FIG. 13
TG/DTG data of pure FAU (solid line) and HBT-FAU nanocrystals (dotted line) (10 °C min^{-1} heating rate, in air)

a few picoseconds, associated with a vibrational relaxation of HBT in FAU samples.

CONCLUSIONS

The crystallization process of pure siliceous and aluminosilicate Beta-type nanocrystals from precursor colloidal mixtures was studied by *in situ* DLS. The nanoscopic entities provided by the silica sources and the particle size distributions during the transformation from amorphous into crystalline particles were studied. Nucleation occurs in amorphous gel particles and growth proceeds *via* solution transfer of soluble species such as silicate anions. The small subcolloidal particles are consumed during the hydrothermal treatment and transformed into crystalline Beta particles with a size of *ca* 60 nm. The combination of IR, DLS, and TEM with the XRD techniques provides details about the early stages of amorphous particles formation and zeolite crystallization.

Nanoscale zeolites such as those above are being used as building blocks for the seeded growth of thin microporous films with controlled morphology and crystal orientation, and for preparation of layers *via* spin-coating approach. The crystal growth of zeolite nanoparticles in solution and thin films was investigated simultaneously, by grazing incidence diffraction using synchrotron radiation. The change of zeolite crystal orientation within the film structure could be followed with the high depth sensitivity of the GID technique. This work also shows that it is possible to determine the crystal orientation in nanoscale polycrystalline zeolite films deposited by both methods spin coating and seed approach. Preferred orientation of porous materials in the films can be obtained by applying non-spherical nanoparticles and different deposition techniques. The present methods are particularly suitable for applications requiring rapid deposition of porous thin films under gentle processing conditions with high degree of density and low roughness.

Finally, microporous nanosized materials serve as hosts for inclusion of the dye 2-(2′-hydroxyphenyl)benzothiazole into a supercage of FAU zeolite. The inclusion process appears to involve a complex interaction between the organic template used for preparation of FAU nanocrystals (TMA^+) and HBT as a co-template occurring during the synthesis. The trans keto tautomer of the dye molecule exhibits highly intensive fluorescence in the zeolite as compared with the cis keto tautomer formed in ethanolic solution.

The nanosized microporous materials with fine particles and immense specific surface areas would affect their magnetic, optical, electric, adsorption, catalytic, and other properties.

I thank Prof. T. Bein, Dr T. H. Metzger, Dr V. De Waele, Dr N. Olson, N. Petkov, M. Reinelt and M. Hölzl for their help and very fruitful discussions, as well as the Bavarian-French Foundation, DFG-CNRS and the ESRF Grenoble for partial financial support.

REFERENCES

1. Szostak R.: *Molecular Sieves – Principles of Synthesis and Identification*. Blakie Academic & Professional, London 1998.
2. Persson A. E., Schoeman B. J., Sterte J., Otterstedt J.-E.: *Zeolites* **1994**, *14*, 557.
3. Schoeman B. J., Sterte J., Otterstedt J.-E.: *Zeolites* **1994**, *14*, 110.
4. Tsapatsis M., Lovallo M., Okubo T., Davis M. E.: *Mater. Res. Soc. Symp. Proc.* **1995**, *371*, 21.
5. Camblor M. A., Corma A., Misfud A., Perez-Pariente J., Valencia S.: *Progress in Zeolites and Microporous Materials* (H. Chon, S.-K. Ihm and Y. S. Uh, Eds); *Stud. Surf. Sci. Catal.* **1997**, *105A*, 341.
6. Mintova S., Olson N. H., Senker J., Bein T.: *Angew. Chem., Int. Ed.* **2002**, *41*, 2558.
7. Kirschhock C. E. A., Ravishankar R., van Looveren L., Jacobs P. A., Martens J. A.: *J. Phys. Chem. B* **1999**, *103*, 4972.
8. Regev O., Cohen Y., Kehat E., Talmon Y.: *Zeolites* **1994**, *14*, 314.
9. Schoeman B. J.: *Microporous Mesoporous Mater.* **1998**, *22*, 9.
10. Mintova S., Petkov N., Karaghiosoff K., Bein T.: *Microporous Mesoporous Mater.* **2001**, *50*, 121.
11. Burkett S. L., Davis M. E.: *Chem. Mater.* **1995**, *7*, 920.
12. Shi J., Anderson M. W., Carr S.-W.: *Chem. Mater.* **1996**, *8*, 369.
13. Tsapatsis M., Lovallo M., Davis M. E.: *Microporous Mater.* **1996**, *5*, 381.
14. Cundy C. S., Cox P. A.: *Chem. Rev.* **2003**, *103*, 663.
15. Schoeman B. J.: *Zeolites* **1997**, *18*, 97.
16. Twomey T. A. M., Mackay M., Kuipers H. P. C. E., Thompson R. W.: *Zeolites* **1994**, *14*, 162.
17. Kirschhock C. E. A., Ravishankar R., Verspeurt F., Grobet P. J., Jacobs P. A., Martens J. A.: *J. Phys. Chem.* **1999**, *103*, 4965.
18. Burkett S. L., Davis M. E.: *J. Phys. Chem.* **1994**, *98*, 4647.
19. de Moor P.-P. E. A., Beelen T. P. M., van Santen R. A.: *J. Phys. Chem.* **1999**, *103*, 1639.
20. de Moor P.-P. E. A., Beelen T. P. M., van Santen R. A., Beck L. W., Davis M. E.: *J. Phys. Chem.* **2000**, *104*, 7600.
21. Walton R. I., Millange F., O'Hare D., Davies A. T., Sanker G., Catlow C. R. A.: *J. Phys. Chem.* **2001**, *105*, 83.
22. Walton R. I., O'Hare D.: *J. Phys. Chem.* **2001**, *105*, 91.
23. Mintova S., Olson N., Valtchev V., Bein T.: *Science* **1999**, *283*, 958.
24. Mintova S., Olson N., Bein T.: *Angew. Chem., Int. Ed.* **1999**, *38*, 3201.

25. Terasaki O.: *Molecular Sieves: Science and Technology* (H. G. Karge and J. Waitkamp, Eds), Vol. 2. Springer, Berlin 1999.
26. Bein T.: *Chem. Mater.* **1996**, *8*, 1636.
27. a) Hedlund J., Schoeman B. J., Sterte J.: *Chem. Commun.* **1997**, 1193; b) Valtchev V: *Chem. Matter.* **2002**, *14*, 4371.
28. Lovallo M. C., Tsapatsis M.: *Chem. Mater.* **1996**, *8*, 1579.
29. Engström V., Mihailova B., Hedlund J., Holmgren A., Sterte J.: *Microporous Mesoporous Mater.* **2000**, *38*, 51.
30. Mintova S., Bein T.: *Adv. Mater. (Weinheim, Ger.)* **2001**, *13*, 1880.
31. Sterte J., Mintova S., Zhang G., Schoeman B. J.: *Zeolites* **1997**, *18*, 387.
32. Clet G., Jansen J. C., van Bekkum H.: *Chem. Mater.* **1999**, *11*, 1696.
33. Xu X., Yang W., Liu J., Lin L.: *Adv. Mater. (Weinheim, Ger.)* **2000**, *12*, 195.
34. Matsufuji T., Nishiyama N., Ueama K., Matsukata M.: *Microporous Mesoporous Mater.* **1999**, *32*, 159.
35. Metzger T. H., Kegel I., Paniago R., Peisl J.: *J. Phys. D.: Appl. Phys.* **1999**, *32*, 202.
36. Chou P. T., Martinez M. L., Studer S. L.: *Appl. Spectrosc.* **1991**, *45*, 918.
37. Stein M., Keck J., Waiblinger F., Kramer H. E. A., Hartschuh A., Port H., Leppard D., Rytz G.: *J. Phys. Chem. A* **2002**, *106*, 2055.
38. Kubo Y., Maeda S., Tokita S., Kubo M.: *Nature* **1996**, *382*, 522.
39. Baerlocher Ch., Meier W. M., Olson D. H.: *Atlas of Zeolite Framework Types*. Elsevier, Amsterdam 2001.
40. Hiemenz P. C., Rajagopalan R.: *Principles of Colloid and Surface Chemistry*. Marcel Dekker Inc., New York 1997.
41. a) Coudurier G., Naccache C., Vedrine J.: *J. Chem. Soc., Chem. Commun.* **1982**, 1413; b) Mintova S., Mihailova B., Valtchev V., Konstantinov L.: *J. Chem. Soc., Chem. Commun.* **1994**, 1791.
42. Mintova S., Reinelt M., Metzger T. H., Senker J., Bein T.: *Chem. Commun.* **2003**, 326.
43. Schoeman B. J., Babouchkina E., Mintova S., Valtchev V., Sterte J.: *J. Porous Mater.* **2001**, *8*, 13.
44. Metzger T. H., Mintova S., Bein T.: *Microporous Mesoporous Mater.* **2001**, *43*, 191.
45. Treacy M. M. J., Higgins J. B. (Eds): *Collection of Simulated XRD Powder Patterns for Zeolites*. Elsevier, Amsterdam 2001.
46. Dutta P. K., Del Barco B., Shieh D. C.: *Chem. Phys. Lett.* **1986**, *127*, 200.
47. Pfeiffer M., Lenz K., Lau A., Elsaesser T.: *J. Raman Spectrosc.* **1995**, *26*, 607.